# Porous Platinum Electrodes Fabricated by Cyclic Electrodeposition of PtCu Alloy: Application to Implantable Glucose Fuel Cells

Arne Kloke,[†] Christian Köhler,[†] Roland Zengerle,[†,‡] and Sven Kerzenmacher*[,†]

[†]IMTEK - Department of Microsystems Engineering, University of Freiburg, Georges-Koehler-Allee 103, 79110 Freiburg, Germany
[‡]BIOSS — Centre for Biological Signalling Studies, University of Freiburg, 79110 Freiburg, Germany

**S** Supporting Information

**ABSTRACT:** We demonstrate the application of cyclic electrodeposition of PtCu alloy to fabricate porous platinum electrodes for implantable glucose fuel cells. Depending on the number of deposition cycles, electrodes with controllable specific surface area can be fabricated, their roughness factors ranging from 20 (slightly roughened) to 3100 (highly porous). Adjusting the specific surface area of the electrode from low to high determines whether it functions as cathode or anode, respectively. Compared to state of the art, this process is beneficial due to shorter fabrication times, lower temperatures, and the requirement of only one process for the fabrication of both electrodes. Correspondingly fabricated glucose fuel cells showed a power density of 5.1 $\mu$W cm$^{-2}$ under close to physiological conditions, which is an improvement by 16% compared to earlier designs. During continuous operation over 90 days the fuel cell showed a mean continuous decay of about 0.8% per day, which is related to catalyst poisoning at the anode. Future work will thus have to focus on the improvement of long-term stability instead of power density.
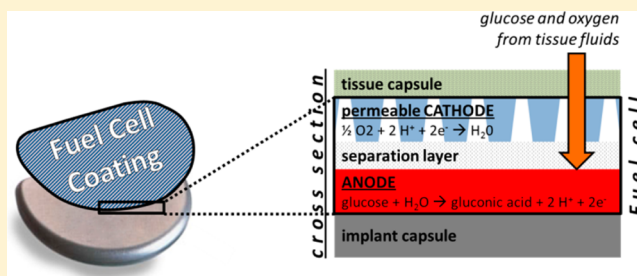
## INTRODUCTION

**Implantable Glucose Fuel Cells.** Implantable glucose fuel cells based on abiotic catalysts are considered as a promising future technology to replace primary batteries as power source for implanted medical microdevices.[1−5] Such fuel cells directly generate electricity from anodic oxidation of glucose and cathodic reduction of dissolved oxygen present in tissue fluids. In contrast to for instance pacemaker batteries, which presently require surgical replacement after 8−10 years, the concept of implantable glucose fuel cells promises a power supply with theoretically unlimited lifetime by continuous harvesting of glucose and oxygen inside the human body. The independence from body motions or temperature gradients is the main advantage of glucose fuel cells over alternative concepts for energy harvesting inside the human body such as mechanical or thermoelectric generators.[1,6] For long-term application of implantable glucose fuel cells, the use of abiotic catalysts such as platinum and carbon is preferable over enzymes or microorganisms since abiotic catalysts pose a low risk of infection, allow for simple steam sterilization, and in contrast to enzymes do not suffer from progressing denaturation and the associated loss of activity and thus inherently limited lifetime.[1,7]

When operated at optimal conditions (e.g., in alkaline media) abiotic glucose fuel cells have been shown to exhibit power densities of up to 20 mW cm$^{-2}$.[8−10] This is different for fuel cells intended for implantation: Here reactant concentrations, pH, and temperature are predefined by the physiological environment. For instance, when implanted into muscle tissue (e.g., near or with a pacemaker), such a fuel cell has to operate at nearly neutral pH, 37 °C, and limited availability of glucose (3−5 mmol L$^{-1}$) and oxygen (~7% oxygen saturation).[11−13] Under such conditions abiotic glucose fuel cells show power densities of only a few $\mu$W cm$^{-2}$.[1−4,14−16] However, this would be sufficient to power a cardiac pacemaker (5−10 $\mu$W) by having a glucose fuel cell installed as a thin layer coating on its capsule surface (15−20 cm$^2$).[17,18] In future, such fuel cells may also be used to supply implanted low-power sensor systems for the monitoring of clinically relevant parameters such as glucose or oxygen concentration, blood pressure, or temperature.[19−22]

**Electrodes for Implantable Glucose Fuel Cells.** A particularly advantageous design for implantable glucose fuel cells is shown in Figure 1.[1] By placing a permeable cathode in front of the anode, reactant access occurs from only one side, allowing for direct placement of the fuel cell onto the exterior surface of an implant capsule. In a tissue environment both electrodes are exposed to the same reactant mixture (surrounding tissue fluid) which simultaneously contains glucose and oxygen. In case nonselective electrode catalysts such as platinum are used, which are highly active toward glucose oxidation and oxygen reduction, this can lead to the formation of mixed electrode potentials and consequently to a drastic decrease in cell voltage.

The state-of-the-art solution to this problem is to use electrodes of different specific surface areas: When using
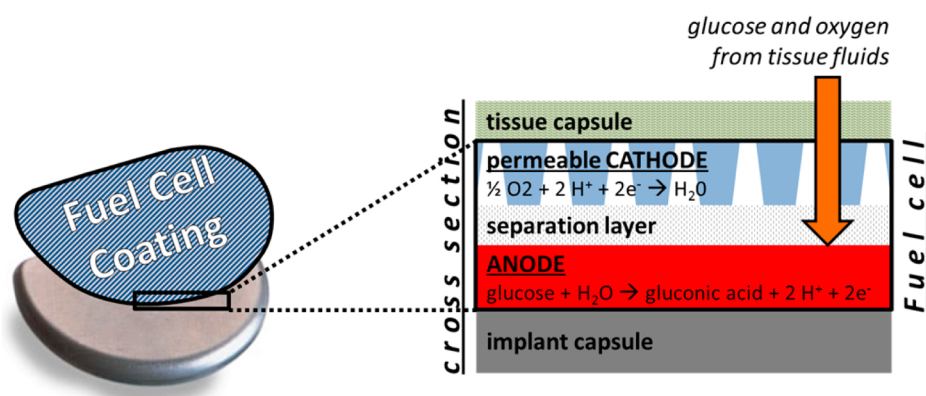
**Figure 1.** Medical implant with a fuel cell coating. The enlarged cross sections on right shows the stacked layers of the fuel cell coating: A separation layer (e.g., highly permeable membrane) is placed in between anode and permeable cathode layer to ensure electrical insulation while allowing for reactant diffusion to the anode. As consequence to the implantation a tissue capsule resulting in a mass transport resistance will form around the overall device. In experiments this is accounted for by placing a filter membrane in front of the fuel cell assembly.

electrodes of low specific surface area under physiological conditions, the electrode potential is dominated by the diffusion-controlled oxygen reduction reaction, whereas electrodes of high specific surface area are dominated by the kinetically controlled glucose oxidation reaction.[23−25] This effect is attributed to oxygen depletion inside the pores of the electrode structure resulting from long diffusion pathways and the substantially lower concentration of oxygen (7% oxygen saturation $\sim 10^{-5}$ mmol $L^{-1}$) compared to glucose ($10^{-3}$ mmol $L^{-1}$).[12,13] In past works such platinum electrodes with different specific surface area for implantable glucose fuel cells have been fabricated by dealloying of thermally alloyed bilayers using different alloying partners such as zinc, aluminum, and nickel.[15,26,27] Unfortunately, this fabrication strategy usually requires high process temperatures (200−1500 °C) and long process times (>1 day for highly porous electrodes) and suffers from low platinum utilization.

Recently, we introduced cyclic electrodeposition of PtCu alloy as a facile method for the fabrication of porous platinum electrodes with adjustable specific surface area. Resulting electrodes showed roughness factors (RF, ratio between active surface area and geometrical base area) ranging from 21 (layer thickness: $0.10 \pm 0.01$ $\mu m$) to higher than 3070 (layer thickness: $19.1 \pm 4.4$ $\mu m$). This process is based on the cyclic alternation of platinum−copper alloy deposition and dissolution of copper from the codeposited alloys, leaving behind a porous platinum structure that grows with each cycle. The residual surface-near copper content (determined by X-ray photoelectron spectroscopy) amounts to 3−6%.[25]

In the present publication, we now investigate the application of this process for the fabrication of both anode and cathode of implantable glucose fuel cells. The relationship between specific surface area and the electrochemical electrode characteristics (open circuit potential, electrode polarization, degradation behavior) is analyzed in half-cell configuration under operation conditions relevant for implantable glucose fuel cells (phosphate buffered saline, 3 mmol $L^{-1}$ glucose, 0.0%−7.0% oxygen saturation). On the basis of these half-cell experiments, we derived an advantageous anode and cathode configuration which is assembled to a complete glucose fuel cell and characterized in terms of power density and operational stability over a period of 90 days.

## ■ EXPERIMENTAL SECTION

**Electrode Fabrication.** Substrates for electrode fabrication were prepared by evaporating titanium (50 nm) and platinum (250 nm) onto a silicon wafer (4 in. diameter, n⁺-doped silicon wafer, 525 $\mu m$ thickness). Photolithography was used to structure the metallization into a defined electrode area (1 cm², if not specified otherwise) with two contact pads for separate connection of current and potential wires. For cathodes in half-cell and fuel cell experiments, metallized silicon wafer pieces (geometric area 1.5 × 1.5 cm²) with 50 $\mu m$ wide KOH-etched tapered feedholes were used as permeable cathode substrates (see elsewhere[23] for details on substrate fabrication). The percentage of the feedholes on the total electrode area was about 8%. Before use all substrates were cleaned in acetone, isopropyl alcohol, and deionized water. The electrode substrates were assembled with two platinum wires (100 $\mu m$ diameter, Chempur, Karlsruhe, Germany) into a sample holder made from polycarbonate and silicone layers, enabling fixation and wire connection as shown elsewhere.[28] Ten cyclic voltammetry (CV) scans (50 mV $s^{-1}$, 1.400 to −0.400 V vs SCE; saturated calomel electrode) were applied in sulfuric acid (0.5 mol $L^{-1}$, Merck, Darmstadt, Germany) to electrochemically clean the substrates surface before deposition. Subsequently, electrode assemblies were transferred into 50 mL of the deposition electrolyte containing sulfuric acid (0.5 mol $L^{-1}$) with additions of $H_2PtCl_6$ (0.02 mol $L^{-1}$, Chempur, Karlsruhe, Germany) and $CuSO_4$ (0.02 mol $L^{-1}$, Merck, Darmstadt, Germany).

Deposition was conducted by CV scans (50 mV $s^{-1}$, 1.400 to −0.600 V vs SCE). Electrodes of different specific surface area were fabricated by variation of the number of deposition cycles ($N_{DC}$). Electrode configurations are named within this paper according to the number of applied deposition cycles, e.g. "5 $N_{DC}$ electrode" when fabricated by 5 deposition cycles. For comparison to state of the art we also fabricated Raney-platinum film anodes (dealloyed from a thermally alloyed bilayer of zinc electrodeposited onto a platinum foil) as described elsewhere.[27]

To clean the electrodes after fabrication, 10 CV scans (50 mV $s^{-1}$, 1.400 to −0.400 V vs SCE) were performed in sulfuric acid (0.5 mol $L^{-1}$). Further scans were applied to determine the electrochemically active surface area of the platinum electrodes. Here, individually adjusted negative scan

limits and slow scan speeds ($\leq 2$ mV s$^{-1}$) were used to precisely determine the desorption current related to a hydrogen monolayer coverage of the active surface area.[29]

Cleaning, fabrication, and characterization experiments were performed with two potentiostat systems (PCI4/300, Gamry Instruments, Warminster, PA, and Solatron 1470E Cell Test System, Ametek, Farnborough, UK) in combination with platinum counter electrodes and saturated calomel reference electrodes (SCE, KE11, Sensortechnik Meinsberg, Ziegra-Knobelsdorf, Germany). All experiments were performed under a nitrogen atmosphere.

**Assemblies for Half-Cell and Fuel Cell Experiments.** In half-cell experiments for the investigation of general and anode properties the same assembly was used as described for electrode fabrication (geometric electrode area of $1.0 \times 1.0$ cm$^2$). For cathode-specific investigations a 140 $\mu$m thick filter membrane with 450 nm pores (Supor-450, Pall Life Sciences, East Hill, NY) was additionally placed in front of the cathodes (geometric area of $1.5 \times 1.5$ cm$^2$) to account for the transport resistance expected from tissue encapsulation of the implanted fuel cell device.[26,30]

For fuel cell experiments a module consisting of six fuel cells connected in parallel was assembled (total footprint area of the fuel cell: 13.5 cm$^2$). For this fuel cell module enlarged anode substrates were used compared to in half-cell experiments which have the same geometric area as the cathodes ($1.5 \times 1.5$ cm$^2$ each instead of $1.0 \times 1.0$ cm$^2$). Each fuel cell was assembled in so-called depletion design as depicted in Figure 1. Also in this case a Supor-450 filter membrane was placed in front of the cathode to simulate expected oxygen transport resistance due to tissue encapsulation. A second Supor-450 filter membrane was used in between cathode and anode to ensure electrical insulation (see Figure 1).

All experiments in half-cell configuration and with complete fuel cells were performed under sterile conditions (established by steam sterilization for 15 min at 121 °C before the first experiment) in aseptic electrochemical reactors.[28] These reactors allow for complete media exchange and for controlled oxygen saturation levels by continuous purging with defined nitrogen-air mixtures. An SCE reference electrode was placed in the center of the reactor. Up to six sample holders for half-cell experiments or one fuel cell module can be placed within one reactor. Unless stated otherwise, all experiments were conducted at 37 °C in freshly prepared phosphate buffered saline (PBS, pH = 7.4, Cl$^-$ concentration of 0.143 mol L$^{-1}$, Invitrogen, Karlsruhe, Germany) containing 3 mmol L$^{-1}$ of $\alpha$-D(+)-glucose monohydrate (Carl-Roth, Karlsruhe, Germany), which corresponds to the expected situation in body tissue.[12,13] Anodes were additionally tested in a chloride-free phosphate buffer (PB, pH = 7.4, 33.9 mmol L$^{-1}$ NaH$_2$PO$_4$ and 116.1 mmol L$^{-1}$ Na$_2$HPO$_4$) to reveal the influence of chloride ions.

**Electrochemical Characterization Procedures.** To obtain reproducible data when performing multiple experiments with the same electrodes, each electrode underwent an electrode regeneration procedure before individual experiments, consisting of potential cycling and subsequent media exchange. Potential cycling (CV scans, 5−10 cycles, 10 mV s$^{-1}$, 1.200 to −0.900 V vs SCE) is conducted to enforce oxidation and desorption of residual adsorbents. In Figure S1 of the Supporting Information we show 20 CV scans recorded with a 500 $N_{DC}$ anode after it was used in a 10 day continuous load experiment (7.0% oxygen saturation). The peak current

densities (peak 1 and peak 2) obtained for anodic glucose oxidation peaks saturate after about 8 CV scans, indicating a recovered, constant catalytic activity. In combination with an exchange of the complete media this procedure thus allows for comparable initial conditions at the beginning of each individual experiment. After performing the electrode regeneration procedure anodes were held at open circuit for 18 h before loads were applied to account for the slow stabilization of electrode potentials. For cathode and fuel cell tests even longer times of 2 days were waited.

*Oxygen sweep experiments* were performed by stepwise increase of the oxygen level from 0.0 to 21.0% oxygen saturation at open circuit. Initially, open circuit potentials (OCP) were recorded for 1.5 days at 0.0% oxygen saturation to allow for constant and thus reproducible electrode potentials. Subsequently, the oxygen saturation level was increased every 3 h. For each step the average OCP of the last 20 min were used for data evaluation.

During *polarization curve experiments*, galvanostatic loads were successively increased every 6 h by 2 $\mu$A cm$^{-2}$ from 0 to 20 $\mu$A cm$^{-2}$. The final value recorded after 6 h at a given load current density was used to construct polarization curves.

All *continuous load experiments* were performed at a current density of 10 $\mu$A cm$^{-2}$. In case of cathodes no regeneration procedure was performed before starting the continuous load experiments, since no degradation was observed after the load curve experiments which were executed right before. During all experiments, the application of galvanostatic loads and data acquisition was performed with our parallel electrochemical testing environment which has been described elsewhere in detail.[28]

## ■ RESULTS AND DISCUSSION

**Dependence of Open Circuit Potential on Specific Surface Area.** Figure 2 shows the dependence of open circuit electrode potentials (OCP) in PBS containing 3 mmol L$^{-1}$ glucose on the number of deposition cycles and the associated specific surface area (expressed as roughness factors, RF). Here,
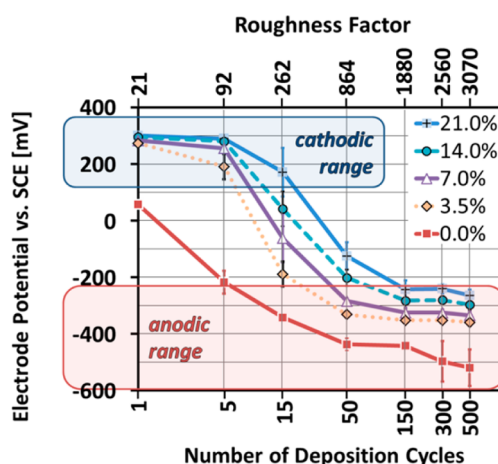


**Figure 2.** Oxygen sweep experiments. Electrode potential vs SCE under open circuit conditions and different oxygen concentrations, shown in dependence on the electrode roughness factor and number of deposition cycles, respectively. Data were recorded at 37 °C in PBS containing 3 mmol L$^{-1}$ glucose. Plotted values and error bars represent the mean value of two samples tested in parallel and their deviation from the mean value, respectively.
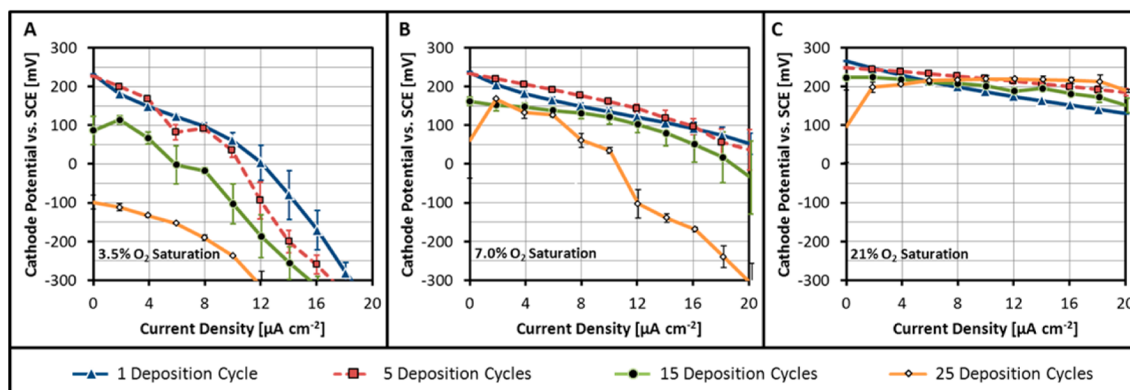
**Figure 3.** Load-curve experiments at 3.5%, 7.0%, and 21.0% oxygen saturation. Comparison of cathodes fabricated with different number of deposition cycles in PBS with glucose (3 mmol L$^{-1}$) at 37 °C. Cathode potential was observed for 6 h at each current density. Plotted values and error bars represent the mean value of two samples tested in parallel and their deviation from the mean value, respectively.

two trends are observable: first, an increase in oxygen saturation leads to more positive electrode potentials; second, an increase in specific surface area of the electrode results in more negative electrode potentials. Both observations result from the simultaneous presence of both reactants — glucose and oxygen — at the electrodes. Consequently, a mixed electrode potential forms at the electrodes which is governed by the balance of glucose oxidation and oxygen reduction. An increase in oxygen concentration leads to an increasing dominance of oxygen reduction over glucose oxidation. Accordingly, the electrode potential shifts toward the more positive redox potential of oxygen reduction.

The more negative electrode potentials with increasing specific surface area are a consequence of the different reaction kinetics of oxygen reduction and glucose oxidation and the different reactant concentrations in tissue environment. At smooth electrode structures (low specific surface area) the oxygen reduction dominates the electrode potential, indicating faster reaction kinetics of oxygen reduction compared to glucose oxidation. When increasing the internal surface area, oxygen depletion occurs along the diffusion pathways to the inside of the porous electrode structure. This oxygen depletion is a consequence of the low oxygen concentration under physiological conditions ($\sim 10^{-5}$ mol L$^{-1}$) compared to glucose ($3 \times 10^{-3}$ mol L$^{-1}$). Thus, only the outmost parts of the catalyst surface are affected by oxygen, and consequently the deeper parts of the internal catalyst surface are dominated by glucose reduction according to the significantly higher availability of glucose.

Accordingly, electrodes fabricated with up to five deposition cycles show OCPs typical for oxygen reduction cathodes of implantable glucose fuel cells, whereas electrodes with 150 and more deposition cycles exhibit open circuit potentials typical for glucose oxidation anodes. The electrodes fabricated by 15 and 50 deposition cycles cannot clearly be assigned to one group. In particular, 15 $N_{DC}$ electrodes markedly change their character from anodic to cathodic in dependence of oxygen concentration.

In the following we analyze the suitability of electrodes fabricated with up to 25 deposition cycles for use as cathodes and electrodes fabricated with 50 and more deposition cycles for use as anodes.

**Cathode: Polarization Curves.** Figure 3 shows polarization curves of cathodes fabricated with 1 to 25 deposition cycles, recorded at 3.5%, 7.0%, and 21.0% oxygen saturation in

PBS containing 3 mmol L$^{-1}$ glucose. At 7.0% oxygen saturation, cathodes fabricated with 1 and 5 deposition cycles exhibit a higher OCP than those fabricated with 15 or 25 deposition cycles. As outlined in the previous section, this can be explained by the increasing influence of glucose oxidation on the electrode potential with increasing specific surface area (see also Figure 2). For increasing current densities the typical curve progression known for polarization curves can be observed with activation, polarization, and mass transport losses.[31] Whereas the OCP increases for decreasing specific surface area, the polarization slope (area specific resistance) increases with decreasing specific surface area due to increasing local current densities. Consequently, 15 $N_{DC}$ cathodes show a reduced slope compared to 1 $N_{DC}$ and 5 $N_{DC}$ cathodes, but their significantly lower OCP prevents 15 $N_{DC}$ cathodes from showing overall higher potentials compared to 1 $N_{DC}$ and 5 $N_{DC}$ cathodes during the polarization curve recorded at 7.0% oxygen saturation. At high current densities (>14 $\mu$A cm$^{-2}$) an accelerated and nonlinear potential decrease is observed, reflecting the limitation in mass transport. According to longer diffusion pathways, this effect is more prominent for electrodes with higher specific surface area.

As shown previously, the maximum power density of glucose fuel cells operated under comparable conditions typically occurs in the range of 10−14 $\mu$A cm$^{-2}$.[24] Within this current density range, electrodes fabricated with 5 deposition cycles show the most positive cathode potential and therefore promise the highest power density when used in complete fuel cells. For 25 $N_{DC}$ cathodes no smooth polarization curve could be recorded. Here, the electrode potential did not stabilize within the recorded 6 h after the load has been increased. This is attributed to oxygen depletion along the pores inside the interior of the electrode structure, occurring due to the longer diffusion pathway in the 25 $N_{DC}$ cathodes compared to electrodes of lower specific surface area.

Similar curve progressions were obtained when polarization curves were recorded at reduced (3.5%) and increased (21.0%) oxygen saturation (see Figure 3A,C). Decreasing oxygen concentration has the effect of increasing polarization slope and the occurrence of mass transport limitation at lower current densities. The most significant change in curve progression is observable for 25 $N_{DC}$ cathodes: Whereas at low oxygen availability (3.5−7.0% oxygen saturation) they do not show typical cathode potentials, cathode potentials in the range of the
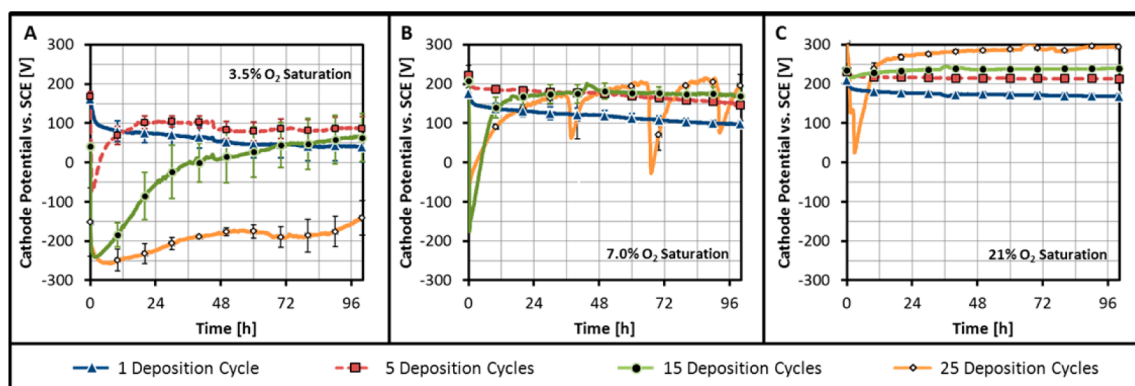
**Figure 4.** Cathode transients under continuous galvanostatic load of 10 $\mu$A cm$^{-2}$ recorded at 37 °C in PBS with 3 mmol L$^{-1}$ glucose. Plotted values and error bars represent the mean value of two samples tested in parallel and their deviation from the mean value, respectively.
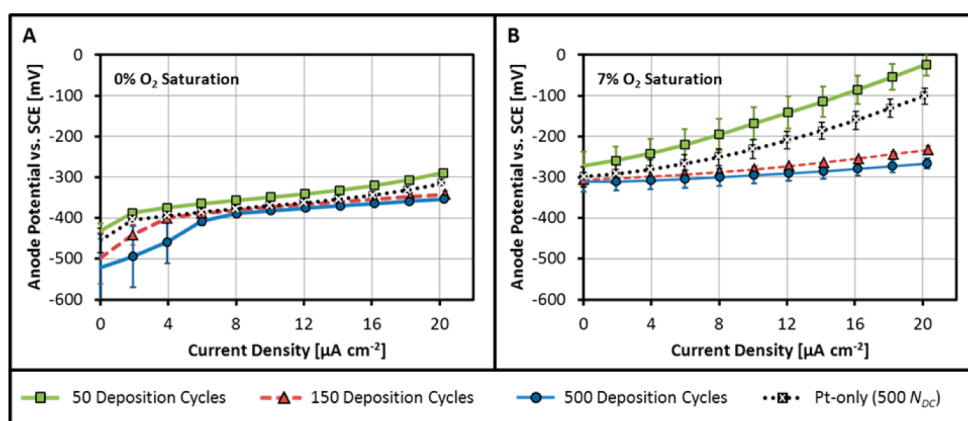


**Figure 5.** Anode polarization curves at 0.0% and 7.0% oxygen saturation. Comparison of anodes fabricated with different number of deposition cycles in PBS with glucose (3 mmol L$^{-1}$) at 37 °C. Anode potentials were observed for 6 h at each galvanostatic load level. Plotted values and error bars represent the mean value of two samples tested in parallel and their deviation from the mean value, respectively.

other cathode configurations and higher are observed for at 21.0% oxygen saturation.

**Cathodes: Transient Behavior under Continuous Load.** Figure 4 shows the evolution of cathode potentials over time at a continuous load current density of 10 $\mu$A cm$^{-2}$, recorded at oxygen saturations of 3.5%, 7.0%, and 21.0%. At 7.0% oxygen saturation 1 $N_{DC}$ and 5 $N_{DC}$ cathodes show a similar curve progression: Because of electrode polarization, a decrease in cathode potential is observed after load application. According to the lower specific surface area and thus higher local current density, the polarization caused decrease in cathode potential is stronger for 1 $N_{DC}$ compared to 5 $N_{DC}$ cathodes.

Fifteen $N_{DC}$ and 25 $N_{DC}$ cathodes show a different curve progression. Here, a drastic potential breakdown by more than 250 mV occurs when the current density is increased from 0 to 10 $\mu$A cm$^{-2}$. Subsequently, the potential of 15 $N_{DC}$ cathodes relaxes within 1.5 days to a constant potential which is even more positive than the potential of 1 $N_{DC}$ and 5 $N_{DC}$ cathodes. For 25 $N_{DC}$ cathodes the highest cathode potentials are observed among all investigated configurations. Unfortunately, their high susceptibility to any changes in oxygen supply or load do not allow for a reliable power generation.

At reduced oxygen saturation (3.5%) lower cathode potentials are observed for all electrodes compared to at 7.0% (see Figure 4A). Except during the first 12 h, the highest cathode potential is observed for 5 $N_{DC}$ cathodes. At this

oxygen concentration 5 $N_{DC}$ cathodes are also affected by a slow potential relaxation behavior after load application (compare 15 $N_{DC}$ and 25 $N_{DC}$ cathodes in Figure 4B). Moreover, a significantly longer relaxation time is observed for 15 $N_{DC}$ cathodes at 3.5% compared to at 7.0% oxygen saturation. At this oxygen level 25 $N_{DC}$ cathodes show a potential that is too negative for practical application in the glucose fuel cell.

In consistence with the previous observations, an increase in oxygen saturation (21.0%) leads to in general higher cathode potentials compared to at 7.0% (see Figure 4C). Here, 25 $N_{DC}$ cathodes show the highest potentials and thus best performance. Moreover, the time scale of the potential relaxation after load application observed for 15 $N_{DC}$ and 25 $N_{DC}$ cathodes is significantly reduced.

Overall, these continuous load experiments show that there is not a single best electrode configuration. The specific surface area of cathodes has to be adjusted in dependence of the present oxygen concentration. Electrodes of low specific surface area allow for more positive OCP values but suffer from higher electrode polarization due to higher local current densities compared to cathodes of high specific surface area. On the other hand, high specific surface area cathodes suffer from oxygen depletion along their pores (long diffusion pathways) and thus require high oxygen concentrations to supply oxygen to all over their surface area and thus to obtain high cathode potentials. Therefore, the potential-relaxation phenomenon
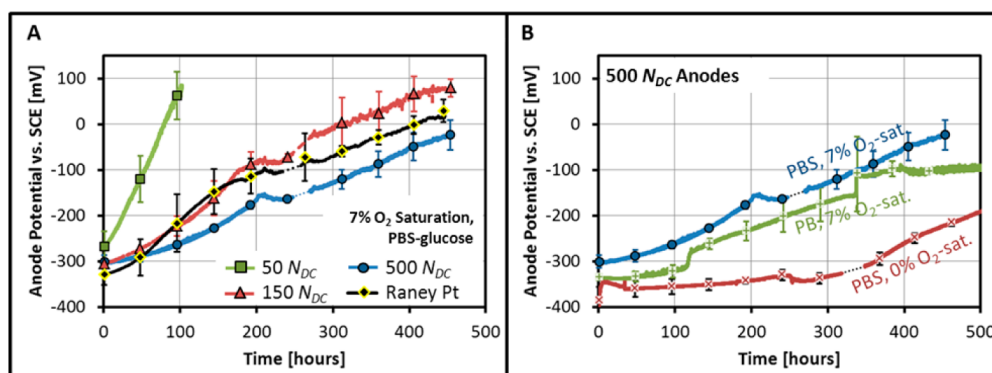
**Figure 6.** Anode potential transients at a continuous galvanostatic load of 10 $\mu$A cm$^{-2}$. (A) Comparison of anodes fabricated with different number of deposition cycles to state of the art Raney-platinum film anodes (labeled "Raney-Pt"), all tested in PBS with 3 mmol L$^{-1}$ glucose at 7.0% oxygen saturation at 37 °C. (B) Comparison of 500 $N_{DC}$ anodes when operated in phosphate buffer with (PBS) and without chloride (PB). Plotted values and error bars represent the mean value of two samples tested in parallel and their deviation from the mean value, respectively.

**Table 1. Average Anode Potential Drift Rates (Given in mV day$^{-1}$) within the First 240 h (10 days)$^a$**

| anode | 50 $N_{DC}$ | Pt-only (Pt- black) | 150 $N_{DC}$ | 300 $N_{DC}$ | 500 $N_{DC}$ | PtZn-Raney anode |
|---|---|---|---|---|---|---|
| PBS, 7.0% O$_2$-sat. | 65 ± 7$^b$ | 58 ± 2$^c$ | 23 ± 1 | 19 ± 2 | 14 ± 1 | 26 ± 4 |
| PBS, 0.0% O$_2$-sat. | 25 ± 9$^b$ | 34 ± 14$^c$ | 3 ± 3 | 7 ± 9 | 6 ± 8 | 9 ± 4 |
| PB, 7.0% O$_2$-sat. | 50 ± 7$^b$ | 44 ± 3$^c$ | 23 ± 1 | 18 ± 2 | 14 ± 1 | 26 ± 4 |

$^a$Reduced observation times were applied when the anode potential reached non-typical values for glucose oxidation anodes (>0 mV vs SCE). Listed values and errors represent the mean value of two samples tested in parallel and their deviation from the mean value, respectively. $^b$Reduced observation period of 100 h. $^c$Reduced observation period of 150 h.

occurs and stabilization takes longer time, in particular at lower oxygen concentration and at higher specific surface area (long diffusion pathways). Hence, cathodes with high specific surface area are very sensitive toward changes in oxygen concentration and load.

**Anode: Polarization Curves.** Figure 5 shows polarization curves recorded at 0.0% and 7.0% oxygen saturation for anodes fabricated with different number of deposition cycles. Similar to the cathodes, also the anode OCP and polarization slope decreases with increasing specific surface area. Hence, independent of oxygen concentration or load 500 $N_{DC}$ anodes show the most negative potential and thus best performance for the use in glucose fuel cells of all tested configurations. Electrodes with more than 500 deposition cycles were not considered since already between 300 $N_{DC}$ and 500 $N_{DC}$ no significant improvements were observed in roughness factor as well as in anode potential.

Figure 5 also shows polarization curves of electrodes fabricated with 500 deposition cycles in a Pt-only electrolyte (without addition of copper), which corresponds to a classic platinum-black electrode. The OCP and polarization slope of this anode (Pt-only, RF = 1040 ± 260) ranges between that observed for 50 $N_{DC}$ (RF = 860 ± 70) and 150 $N_{DC}$ (RF = 1880 ± 230) anodes, as expected from the corresponding roughness factors.

At 0.0% oxygen saturation the anode potentials at low current densities are more negative than expected from extrapolation of the data points recorded at higher current densities (see Figure 5A). This observation is not related to activation losses at the electrodes but stems from non-steady-state potentials recorded at low current densities due to a very slow stabilization of the electrode potential (see Figure S2 in Supporting Information). We explain this to be a consequence of the initially pristine electrode surface after the regeneration procedure (potential cycling + media exchange; see Exper-

imental Section). At low currents only small amounts of glucose are oxidized, and not enough oxidation products are produced to obtain a steady-state coverage of the entire electrode surface. At 7.0% oxygen saturation, oxygen as additional electron acceptor is available, leading to a faster turnover of glucose and faster accumulation of reaction products at the electrode surface. Hence, a stabilization of the electrode potential occurs at a faster time scale when oxygen is present, and the corresponding data points in the polarization curve represent steady-state values.

**Anodes: Continuous Load Experiments.** In Figure 6A, the evolution of anode potentials of different electrodes operated at a continuous galvanostatic load of 10 $\mu$A cm$^{-2}$ over a period of 400 h (18 days) are compared. At any time anodes with higher specific surface area show more negative electrode potentials. Consequently, 500 $N_{DC}$ anodes represent the best configuration for the use in glucose fuel cells. Throughout the observation period, all anodes show a continuous drift toward more positive potentials, indicating poisoning of the catalyst surface. The drift rate is slower for anodes with higher specific surface area, as shown in Table 1. 50 $N_{DC}$ anodes reach potentials above 0 mV vs SCE after only 80 h of operation at 10 $\mu$A cm$^{-2}$. The potential drift behavior of 150 $N_{DC}$ and 500 $N_{DC}$ anodes is comparable to state-of-the-art Raney-platinum film anodes (tested in the same vessel). Discontinuities in curve progression occur due to manual adjustment of purging flow rates and liquid levels in the electrochemical reactor.

To evaluate the influence of oxygen and chloride on the potential drift rate 500 $N_{DC}$ anodes were operated in phosphate buffer with (PBS) and without chloride (PB) and at 7.0% and 0.0% oxygen saturation, as shown in Figure 6B. At 0.0% oxygen saturation a significantly slower drift is observed compared to at 7.0% (see Table 1). This is attributed to accelerated glucose oxidation in the presence of oxygen. At the electrode oxygen is

reduced and thus acts as an additional electron acceptor for glucose oxidation. This also leads to an accelerated production of gluconic acid which is known to poison the catalytically active platinum surface.[32]

To distinguish between degradation caused by the presence of chloride[33,34] and degradation due to the adsorption of glucose oxidation products (mainly gluconic acid[1,32]), we repeated the continuous load experiment in a chloride-free phosphate buffer (PB, pH = 7.4, see Experimental Section). The comparison between the chloride-free PB and PBS (phosphate buffered saline, 0.143 mol L$^{-1}$ Cl$^-$) revealed a constant shift of about 50 mV toward less negative anode potentials in the presence of chloride. No significant influence on the drift rate is observed. Thus, the presence of chloride ions influences the electrode potential formation process (constant drop of cell voltage), but chloride does not cause catalyst poisoning (no drift of the cell voltage).

**Fuel Cells: Selection of Electrode Configurations.** For fuel cell experiments in PBS containing physiological amounts of glucose and oxygen 5 $N_{DC}$ electrodes have been chosen as cathode configuration. After 100 h of continuous operation they not only show the most positive potential at 3.5% oxygen saturation and an only slightly less positive potential at 7.0% oxygen saturation, but also they proved to be significantly less sensitive to changes in load current as compared to 15 $N_{DC}$ or 25 $N_{DC}$ cathodes. 500 $N_{DC}$ electrodes were chosen as anodes for fuel cell experiments, since they exhibited the highest specific surface area and consequently the best performance in oxygen sweep, polarization curve, and continuous load experiments.

**Fuel Cells: Polarization Curves.** In Figure 7, a polarization curve recorded at 7.0% oxygen saturation for a fuel cell module assembled from 5 $N_{DC}$ cathodes and 500 $N_{DC}$ anodes is compared to state of the art fuel cells with Raney-platinum film electrodes.[23] With 5.1 $\mu$W cm$^{-2}$ the tested fuel cell module shows a by 16% higher maximum power density compared to state of the art (see Figure 7C). As can be seen from Figure 7A, this improvement is mainly due to the cathode, where higher current densities are sustainable before substantial mass transport losses occur. This indicates a better accessibility of the electrode surface, meaning a shorter average diffusion pathway in the morphology of the 5 $N_{DC}$ cathodes compared to state of the art Raney-platinum film cathodes.

At 21.0% oxygen saturation, substantial mass transport losses occur only at significantly higher current densities beyond 30 $\mu$A cm$^{-2}$, enabling a maximum power density of 9.3 $\mu$W cm$^{-2}$. Compared to at 7.0% oxygen saturation this is an enhancement of 82%, which clearly confirms previous conclusions about glucose fuel cell systems tested under conditions simulating implantation: The onset of oxygen mass transport limitations is the limiting factor to fuel cell performance.[11,24] This observation has two consequences: First, future research on glucose fuel cells operated under conditions simulating tissue implantation will not enable drastic improvement in power density. Second, concepts for implantation in bloodstream or other locations inside the human body featuring higher oxygen concentrations than in muscle tissue should be evaluated.

Fuel cells in the literature exhibit significantly lower open circuit voltages (160−350 mV)[2,3,5,35,36] than the fuel cell of the present work (Figure 7B, about 600 mV). With up to 2 $\mu$W cm$^{-2}$ at 7% oxygen saturation[2] and up to 5.3 $\mu$W cm$^{-2}$ at 21% oxygen saturation[3] also their power densities are significantly lower than the 5.1 and 9.3 $\mu$W cm$^{-2}$ reached in the present
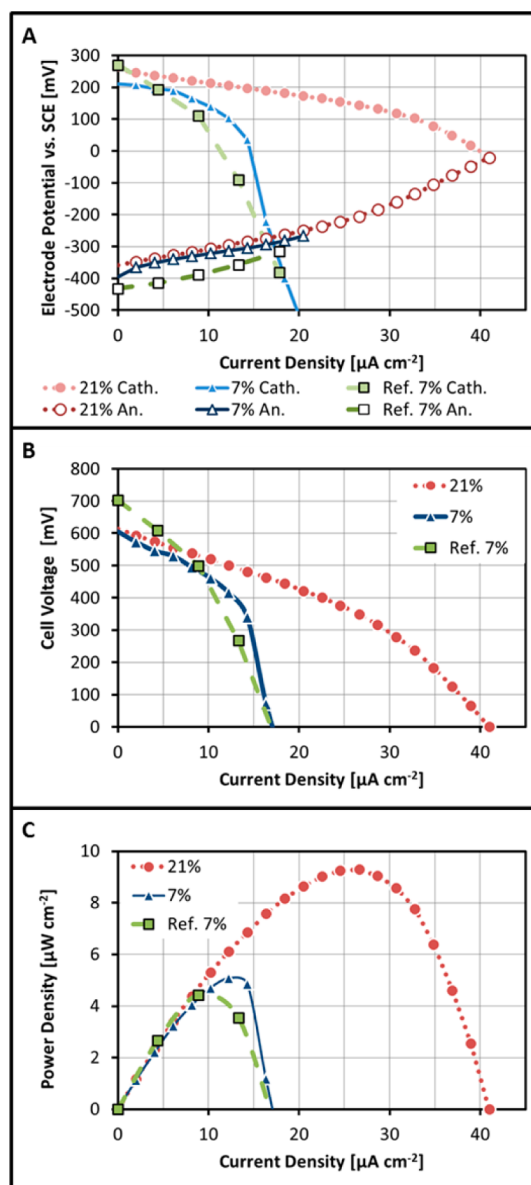


**Figure 7.** Fuel cell polarization curves. (A) Separately recorded cathode and anode potentials, (B) cell voltage, and (C) power density The tested fuel cell module consists out of six interconnected individual fuel cell assemblies (2.25 cm$^2$ base area each) and was characterized at 37 °C in PBS with glucose (3 mmol L$^{-1}$). State-of-the-art data of a fuel cell with Raney-platinum film electrodes[23] are shown as reference (see label "Ref."). Percent values indicate the corresponding oxygen saturation.

work, respectively. It can be assumed that the difference in OCV stems from different anode potentials, which we attribute to a difference in specific surface area. As shown in Figure 2, electrodes with higher specific surface area are less sensitive toward the presence of oxygen and thus exhibit lower potentials. For instance, Oncescu et al. observed an anode OCP of about −160 mV vs SCE at 7% oxygen saturation, which is more than 200 mV less negative than the OCP of our 500 $N_{DC}$ anode (Figure 7).[2] Unfortunately, Oncescu et al. did not report the specific surface area of their electrodes, but with less than 400 nm in thickness their anodes are significantly thinner than the 19 $\mu$m thick 500 $N_{DC}$ anodes[25] and thus most probably show significantly lower specific surface area.

Higher power densities of up to 180 $\mu$W cm$^{-2}$ have been reported by Rapoport et al. However, these were obtained at a current density of 1500 $\mu$A cm$^{-2}$ during a polarization curve recorded at a high scan rate of 10 $\mu$A cm$^{-2}$ s$^{-1}$ (in PBS with 10 mmol L$^{-1}$ glucose, oxygen concentration is not given).[5] Under steady-state conditions such high power densities cannot be realized, since the diffusive mass transport into an implantable fuel cell occurs far too slow compared to the required current densities. As can be seen from Figure 3, current densities of only about 14 $\mu$A cm$^{-2}$ can be drawn from the cathode at 7% oxygen saturation before significant mass transport losses occur. When awaiting steady state (scan rate is not specified in reference) Rapoport et al. therefore only obtained a maximum power density of 3.4 $\mu$W cm$^{-2}$. We observed a similar dependence of the maximum power density on the scan rate when recording polarization curves at high scan rates with our fuel cell module: At a scan rate of 20 and 2000 $\mu$A cm$^{-2}$ s$^{-1}$, it exhibited power density of up to 33 and 190 $\mu$A cm$^{-2}$, respectively (see Figure S3 in Supporting Information).

**Fuel Cells: Degradation Behavior under Continuous Load.** Figure 8 shows the evolution of electrode potentials over
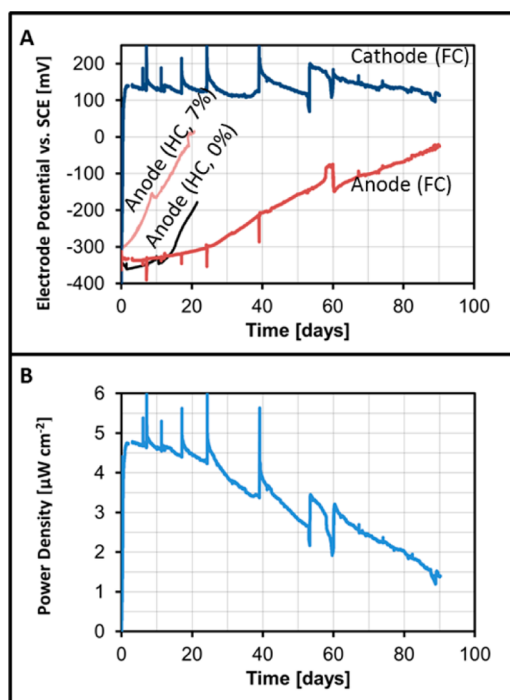


**Figure 8.** Fuel cell continuous load experiments (10 $\mu$A cm$^{-2}$) at 7.0% oxygen saturation. (A) Separately recorded cathode and anode potentials from fuel cell experiments (labeled "FC") are shown in comparison to anode half-cell experiments (labeled "HC") performed at 0.0% and 7.0% oxygen saturation (see Figure 6). (B) Evolution of the power density over time. Peak-like discontinuities in curve progression occur due to manual adjustment of purging flow rates and liquid levels in the electrochemical reactor.

time of a complete fuel cell module operated at 10 $\mu$A cm$^{-2}$. A maximum power density of 4.7 $\mu$W cm$^{-2}$ is observed after nearly 2 days of operation. Subsequent to this maximum, the power density of the fuel cell decreases continuously down to a power density value of 1.5 $\mu$W cm$^{-2}$ after 90 days of operation, which on average corresponds to a drift rate of about 0.036 $\mu$W cm$^{-2}$ day$^{-1}$. This performance decay is mainly due to anode poisoning, as can clearly be seen from the

evolutions of cathode and anode potential, shown in Figure 8B. Nevertheless, the 500 $N_{DC}$ anodes show significantly less drift in fuel cell experiments than in the corresponding half-cell experiments, even when compared to those conducted at 0.0% oxygen saturation. This effect may be related to the filter membranes placed in front of the anode during fuel cell experiments. However, it is not yet understood and thus requires further investigation.

Overall, the continuous load experiments with anodes and fuel cells show no stabilization of the power density during the observation time (90 days). Instead, a continuous decrease in power density is observed, indicating a continuous decrease of catalytic activity (e.g., by adsorbed reaction products) at the electrode surfaces, in particular at the anode. The observed degradation is comparable to previous results with glucose fuel cell electrodes made from carbon and platinum–bismuth nanoparticles embedded in hydrogels.[11] These fuel cells exhibited a comparable cell voltage of about 160 mV after 90 days of operation, and performance degradation was also shown to mainly result from anode poisoning. Similar to the results in Figure 8, after 90 days an anode potential of approximately −50 mV vs SCE was observed at 8.9 $\mu$A cm$^{-2}$ for these fuel cells.

## ■ CONCLUSION

In the present work we demonstrated the application of cyclic electrodeposition of PtCu alloy to the fabrication of porous platinum anodes and cathodes for implantable glucose fuel cells. Compared to the state-of-the-art approach (dealloying of thermally formed PtZn and PtAl alloys[23]), this process is beneficial due to shorter fabrication times, lower temperatures, and the requirement of only one process for the fabrication of both electrodes instead of using different materials and processes. By adjusting the number of deposition cycles, the specific surface area of the electrode can be controlled, which determines whether it functions as cathode or anode of the implantable fuel cell. An optimum specific surface area for cathodes was found to be related to a balance of high surface area (enabling low local current density) and high oxygen accessibility of the entire catalyst surface, which strongly depends on the present oxygen concentration. Anodes were shown to always profit from high specific surface area independent of the present oxygen concentrations. Moreover, the new fabrication process is directly applicable to any conductive surface, and thus future implantable glucose fuel cells could directly be fabricated as a coating on the titanium capsule of medical implants such as cardiac pacemakers. With 5.1 $\mu$W cm$^{-2}$, fuel cells assembled from 5 $N_{DC}$ cathodes and 500 $N_{DC}$ anodes showed a by 16% higher power density at 7.0% oxygen saturation compared to state of the art. These initial power densities would definitely be sufficient to power a cardiac pacemaker (about 16 cm$^2$ surface area, 5−10 $\mu$W,[17,18]). For operation at 21.0% oxygen saturation instead of 7.0% (tissue environment) higher power densities of up to 9.3 $\mu$W cm$^{-2}$ can be achieved. This shows that oxygen availability in a body tissue environment is the limiting factor in power density and thus indicates that for higher power densities fuel cell implantation into the bloodstream should be considered.

However, at present the platinum-based fuel cells suffer from an unsatisfactory long-term stability (reduction in power density of 70% after 90 days). Hence, future research should be focused on long-term stability instead of initial performance. The predominant part of the degradation is related to anode

poisoning. Since the presence of chloride was shown to cause no acceleration in anode degradation, we assume poisoning by adsorbed reaction products to be the major effect. Also, the vulnerability of platinum electrodes to continuous poisoning by reaction products is known from comparable fuel cell systems using small organic molecules as fuels, such as methanol or formic acid. Here the most prominent solution is to use platinum alloy catalyst, in which platinum enables high oxidation rates of the fuel molecules and the alloying partner enables an accelerated desorption of the reaction products.[37−39] Hence, the implementation of comparable catalytic effects in highly porous platinum electrodes should be considered in future research on implantable glucose fuel cells. Moreover, future research is required to clarify the mechanism behind the reduced anode degradation rate which was observed when an additional filter membrane is mounted in front of the anode. Eventually, also the biocompatibility of the here presented electrodes has to be considered. Whereas platinum is widely used in implantable electrodes, catheters, and stents,[40] the presence of residual copper requires a detailed investigation, since several physiological diseases are known to be related to deviant copper levels.[41] Since the fuel cell electrodes will not be in direct contact with the tissue environment, in particular the release of copper ions is of interest. Here, a limited release into tissue fluids might be tolerable since the physiological concentration (e.g., $0.6-1.4$ mg $L^{-1}$ in plasma and serum, $2.45-9.90$ $\mu$g $g^{-1}$ in liver tissue[42]) and the daily tolerable dose of copper ions (0.5 mg per kg body mass[43]) are high in relation to the total copper content of an implantable fuel cell (about 25 mg of copper is embedded in a fuel cell of 20 cm$^2$).

## ASSOCIATED CONTENT

### Ⓢ Supporting Information
Three additional figures, providing further information on the electrode regeneration process (Figure S1), stabilization of electrode potentials during anodic polarization curves (Figure S2), and polarization curve results obtained at high scan rates (Figure S3). This material is available free of charge via the Internet at http://pubs.acs.org.

## AUTHOR INFORMATION

### Corresponding Author
*Tel +49-761-203-73218; Fax +49-761-203-73299; e-mail kerzenma@imtek.uni-freiburg.de.

### Notes
The authors declare no competing financial interest.

## ABBREVIATIONS
CV, cyclic voltammetry; OCP, open circuit potential; OCV, open circuit voltage; PB, chloride-free phosphate buffer; PBS, phosphate buffered saline; RF, roughness factor; SCE, saturated calomel electrode; $N_{DC}$, number of deposition cycles in electrode fabrication.

## REFERENCES
(1) Kerzenmacher, S.; Ducrée, J.; Zengerle, R.; von Stetten, F. *J. Power Sources* **2008**, *182*, 1−17.
(2) Oncescu, V.; Erickson, D. *J. Power Sources* **2011**, *196*, 9169−9175.
(3) Sharma, T.; Hu, Y.; Stoller, M.; Feldman, M.; Ruoff, R. S.; Ferrari, M.; Zhang, X. *Lab Chip* **2011**, *11*, 2460−2465.
(4) Apblett, C. A.; Ingersoll, D.; Sarangapani, S.; Kelly, M.; Atanassov, P. *J. Electrochem. Soc.* **2010**, *157*, B86−B89.
(5) Rapoport, B. I.; Kedzierski, J. T.; Sarpeshkar, R. *PLoS One* **2012**, *7*, e38436.
(6) Lueke, J.; Moussa, W. A. *IEEE Sens. J.* **2011**, *11*, 1433−1460.
(7) Rubenwolf, S.; Kerzenmacher, S.; Zengerle, R.; von Stetten, F. *Appl. Microbiol. Biotechnol.* **2011**, *89*, 1315−1322.
(8) Fujiwara, N.; Yamazaki, S.; Siroma, Z.; Ioroi, T.; Senoh, H.; Yasuda, K. *Electrochem. Commun.* **2009**, *11*, 390−392.
(9) Scott, D.; Liaw, B. Y. *Energy Environ. Sci.* **2009**, *2*, 965−969.
(10) Basu, D.; Basu, S. *Electrochim. Acta* **2010**, *55*, 5775−5779.
(11) Kerzenmacher, S.; Ducrée, J.; Zengerle, R.; von Stetten, F. *J. Power Sources* **2008**, *182*, 66−75.
(12) Maggs, D. G.; Jacob, R.; Rife, F.; Lange, R.; Leone, P.; During, M. J.; Tamborlane, W. V.; Sherwin, R. S. *J. Clin. Invest.* **1995**, *96*, 370−377.
(13) Gough, D. A.; Anderson, F. L.; Giner, J.; Colton, C. K.; Soeldner, J. S. *Anal. Chem.* **1978**, *50*, 941−944.
(14) Drake, R. F.; Kusserow, B. K.; Messinger, S.; Matsuda, S. *Trans. - Am. Soc. Artif. Intern. Organs* **1970**, *16*, 199−205.
(15) Gebhardt, U.; Rao, J. R.; Richter, G. J. *J. Appl. Electrochem.* **1976**, *6*, 127−134.
(16) Rao, J. R.; Richter, G. J.; von Sturm, F.; Weidlich, E. *Bioelectrochem. Bioenerg.* **1976**, *3*, 139−150.
(17) Wong, L. S. Y.; Hossain, S.; Ta, A.; Edvinsson, J.; Rivas, D. H.; Naas, H. *IEEE J. Solid-State Circuits* **2004**, *39*, 2446−2456.
(18) Chandrakasan, A. P.; Verma, N.; Daly, D. C. *Annu. Rev. Biomed. Eng.* **2008**, *10*, 247−274.
(19) Bingger, P.; Fiala, J.; Seifert, A.; Weber, N.; Foerster, K.; Heilmann, C.; Beyersdorf, F.; Woias, P.; Zappe, H. In *Vivo Monitoring of Blood Oxygenation Using an Implantable Mems-Based Sensor*; Proceedings of the IEEE MEMS Conference, 2010, Hong Kong, China, pp 1031−1034.
(20) Fiala, J.; Bingger, P.; Foerster, K.; Heilmann, C.; Beyersdorf, F.; Zappe, H.; Seifert, A. *Implantable Sensor for Blood Pressure Determination via Pulse Transit Time*; Proceedings of the IEEE Sensors Conference 2010, Kona HI, pp 1226−1229.
(21) Darwish, A.; Hassanien, A. E. *Sensors* **2011**, *11*, 5561−5595.
(22) Black, R. D. *IEEE Sens. J.* **2011**, *11*, 3171−3182.
(23) Kerzenmacher, S.; Kräling, U.; Metz, T.; Ducrée, J.; Zengerle, R.; von Stetten, F. *J. Power Sources* **2011**, *196*, 1264−1272.
(24) Kloke, A.; Biller, B.; Kräling, U.; Kerzenmacher, S.; Zengerle, R.; von Stetten, F. *Fuel Cells* **2011**, *11*, 316−326.
(25) Kloke, A.; Köhler, C.; Zengerle, R.; Kerzenmacher, S. *Adv. Mater.* **2012**, *24*, 2916−2921.
(26) Kerzenmacher, S.; Kräling, U.; Schroeder, M.; Brämer, R.; Zengerle, R.; von Stetten, F. *J. Power Sources* **2010**, *195*, 6524−6531.
(27) Kerzenmacher, S.; Schroeder, M.; Brämer, R.; Zengerle, R.; von Stetten, F. *J. Power Sources* **2010**, *195*, 6516−6523.
(28) Kerzenmacher, S.; Mutschler, K.; Kräling, U.; Baumer, H.; Ducrée, J.; Zengerle, R.; von Stetten, F. *J. Appl. Electrochem.* **2009**, *39*, 1477−1485.
(29) Trasatti, S.; Petrii, O. A. *J. Electroanal. Chem.* **1992**, *327*, 353−376.
(30) Sharkawy, A. A.; Klitzman, B.; Truskey, G. A.; Reichert, W. M. *J. Biomed. Mater. Res.* **1997**, *37*, 401−412.
(31) Vielstich, W.; Lamm, A.; Gasteiger, H. *Handbook of Fuel Cells - Fundamentals, Technology, Applications*; John Wiley & Sons: Chichester, 2003; Vol. 1, pp 47−69.
(32) Rao, M. L. B.; Drake, R. F. *J. Electrochem. Soc.* **1969**, *116*, 334−337.
(33) Schmidt, T. J.; Paulus, U. A.; Gasteiger, H. A.; Behm, R. J. *J. Electroanal. Chem.* **2001**, *508*, 41−47.
(34) Skou, E. M. *Acta Chem. Scand.* **1973**, *27*, 2239−2241.
(35) Choi, Y. K.; Wang, G.; Nayfeh, M. H.; Yau, S. T. *Biosens. Bioelectron.* **2009**, *24*, 3103−3107.

19697

dx.doi.org/10.1021/jp306168t | *J. Phys. Chem. C* 2012, 116, 19689−19698

(36) Ryu, J.; Kim, H. S.; Hahn, H. T.; Lashmore, D. *Biosens. Bioelectron.* **2010**, *25*, 1603−1608.

(37) Casado-Rivera, E.; Gal, Z.; Angelo, A. C. D.; Lind, C.; DiSalvo, F. J.; Abruna, H. D. *ChemPhysChem* **2003**, *4*, 193−199.

(38) Tang, W.; Jayaraman, S.; Jaramillo, T. F.; Stucky, G. D.; McFarland, E. W. *J. Phys. Chem. C* **2009**, *113*, 5014−5024.

(39) Kang, S.; Lee, J.; Lee, J. K.; Chung, S. Y.; Tak, Y. *J. Phys. Chem. B* **2006**, *110*, 7270−7274.

(40) Cowley, A.; Woodward, B. *Platinum Met. Rev.* **2011**, *55*, 98−107.

(41) Helsen, J. A.; Breme, H. J. *Metals as Biomaterials*, 1st ed.; John Wiley & Sons: Weinheim, 1998; p 270.

(42) Caroli, S.; Alimonti, A.; Coni, E.; Petrucci, F.; Senofonte, O.; Violante, N. *Crit. Rev. Anal. Chem.* **1994**, *24*, 363−398.

(43) Wiberg, N.; Wiberg, E.; Hollemann, A. *Lehrbuch der Anorganischen Chemie*, 102nd ed.; de Gruyter: Berlin, 2007; p 1434.